Precision Engineering 72 (2021) 717–729

Contents lists available at ScienceDirect

Precision Engineering

journal homepage: www.elsevier.com/locate/precision

Deformation behaviour of soft-brittle polycrystalline materials determined by nanoscratching with a sharp indenter

Weihai Huang, Jiwang Yan *

Department of Mechanical Engineering, Faculty of Science and Technology, Keio University, 3-14-1 Hiyoshi, Kohoku-ku, Yokohama, 223-8522, Japan

ARTICLE INFO

Keywords:
Deformation behaviour
Nanoscratching
Soft brittle material
Polycrystalline material
Sharp indenter

ABSTRACT

Polycrystalline zinc selenide (*p*-ZnSe) is a typical soft brittle material with important optical applications. In this work, single and repeated nanoscratching tests were performed using a Berkovich indenter along the face-forward (FF) and edge-forward (EF) directions. The morphological features of the scratched grooves and the subsurface microstructural changes in the material were characterised by scanning electron microscopy, Raman spectroscopy, and electron backscatter diffraction (EBSD). Material removal in the ductile mode was obtained in the EF scratching direction; this was accompanied by the slip lines, and the radial cracks generated along grain boundaries. In contrast, brittle fractures occurred in the FF scratching direction, resulting in radial and lateral cracks which are responsible for generating the peeling of the material. The EBSD results demonstrated that the {111} planes are the primary slip plane and secondary cleavage plane, whereas the {110} planes are the primary cleavage plane and secondary slip planes. Tensile residual stress was detected in the subsurface region of the grooves scratched along the FF direction, whereas compressive residual stress was detected in the EF scratching direction. Fishbone-like patterns were observed in the scratched grooves under all conditions, while no phase transformation was detected. This study provides insights into the fundamental material removal mechanisms of soft brittle crystals in various abrasive machining processes, such as grinding, lapping, and polishing.

1. Introduction

Many commonly used optical materials, such as calcium fluoride (CaF_2) [1], potassium dihydrogen phosphate (KDP) [2], zinc selenide (ZnSe), zinc sulphide (ZnS) [3], and II–VI compound crystals of HgCdTe [4] and CdZnTe [5], are soft and brittle; consequently, they are very difficult to machine. Ultraprecision cutting and abrasive machining processes such as grinding, lapping, and polishing, which reduce the maximum undeformed chip thickness to the nanoscale, are promising methods for fabricating high-quality surfaces of these materials [6]. In industrial applications, some optical lenses are made of polycrystalline materials to reduce material costs; for example, infrared windows are made of polycrystalline ZnSe (*p*-ZnSe) and ZnS. Ultraprecision cutting of soft brittle polycrystalline materials with high surface integrity is more difficult than that of single crystals [7–9] because the surface is roughened by the grain boundary steps [10].

To improve the surface integrity of these materials, it is essential to understand the mechanisms of material removal and damage formation during these machining processes. Although a few previous studies have reported ultraprecision cutting of soft brittle materials, the available literature on abrasive machining processes is still very limited. Unlike in ultraprecision cutting, where the number and shape of the cutting edge are well defined, in abrasive machining processes, the shape, orientation, and penetration depth of various abrasive grains are distinctly different. Therefore, it is more difficult to clarify the material removal mechanisms of the abrasive machining processes.

Nanoscratching tests have been widely recognised as an effective method for investigating the fundamental material deformation and removal mechanisms of brittle materials [11–13]. This is because a sharp indenter is geometrically similar to a grit on the grinding wheel segment [14], or a nanoscale particle in slurry abrasives used in the polishing [15]. Moreover, the nanoscratching apparatus allows the indenter tip to penetrate the workpiece surface with nanometre precision and scratch it, which is the same level as the material removal in grinding and polishing. Meanwhile, a precise record of force and displacement for the indenter tip can be obtained. From this point of view, nanoscratching is an effective method for investigating abrasive machining mechanisms. The shape and size of the abrasive grit have a

* Corresponding author.
E-mail address: yan@mech.keio.ac.jp (J. Yan).

https://doi.org/10.1016/j.precisioneng.2021.07.016
Received 3 May 2021; Received in revised form 16 June 2021; Accepted 24 July 2021
Available online 28 July 2021

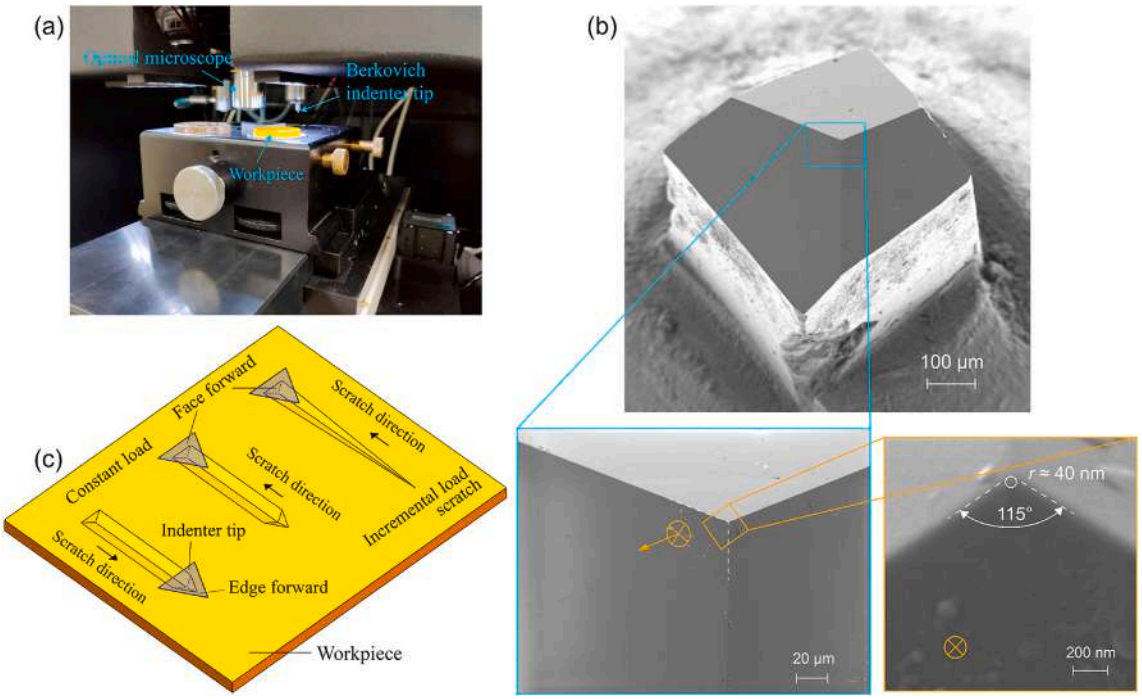

Fig. 1. (a) Photograph of nanoindentation–scratching system for nanoscratching tests. (b) SEM images of the Berkovich indenter tip. (c) Schematic of the nanoscratching process.

great influence on material removal behaviours in abrasive machining process. In general, sharper grits are recommended for ductile abrasive machining of soft brittle materials, while blunter grits are preferable for ductile abrasive machining of hard brittle materials [12,16]. Therefore, nanoscratching tests with a sharp indenter on soft brittle polycrystalline materials are expected to help in improving understanding of the mechanisms of material removal and subsurface damage formation at grain boundaries in abrasive machining.

To date, most of the research on nanoscratching of polycrystals has been performed on materials with high hardness. Borrero-López et al. [17] performed scratch tests on polycrystalline silicon to investigate the fracture response. They found that the grain boundary is not a source of fracture during the scratching of polycrystalline silicon, but it may increase the extent of damage that has already been initiated. Ghosh et al. [18] focused on the investigation of material deformation and damage formation in the scratching of zirconium diboride–silicon carbide (ZrB_2–SiC) composite. They observed that the randomly oriented grains exhibit different extents of microplasticity and that there are different types of damage on the scratched surface, including transgranular fracture in the ZrB_2 phase, fracture at the grain boundary, and interfacial cracking at the ZrB_2–SiC interface. Csanádi et al. [19] investigated the orientation dependence of the scratch resistance of ZrB_2 grains through nanoscratching tests. They reported that, under loads of 50 and 100 mN, the residual scratch depth is significantly affected by the grain orientation, and the ratio of anisotropy of the residual scratch depth is ~30%. Although there has been a large amount of research investigating the material removal and damage formation mechanisms of various materials through the nanoscratching method, to the best of our knowledge, research on nanoscratching of soft-brittle polycrystalline material is extremely limited. Recently, Huang and Yan [20] used a blunt spherical diamond tool to scratch *p*-ZnSe for burnishing micro and nanoscale surface patterns. However, the shape of a blunt spherical indenter is distinctly different from that of abrasive grains used in ultraprecision grinding, lapping, and polishing processes, which have small size, sharp tips, and ridges among different faces.

In this study, single and repeated nanoscratching tests were performed on a *p*-ZnSe workpiece using a sharp Berkovich diamond indenter tip to explore the deformation behaviour of soft-brittle polycrystalline materials in micro and nanoscale abrasive machining processes. The surface morphologies and subsurface damage of scratched grooves for various scratching directions and workpiece crystal orientations under different loading parameters were analysed. It is expected that the findings of this study can help understand the material deformation behaviours of soft-brittle polycrystalline materials associated with crystal orientation and grain boundaries during abrasive machining, which in turn provide guidelines for improving the machined surface integrity.

2. Materials and methods

The experimental workpiece was a *p*-ZnSe wafer prepared by chemical vapor deposition. The workpiece was 25 mm in diameter and 3 mm thick. The grain size of the workpiece ranged from 3 to 80 μm. The workpiece surface was polished to a very smooth finish with a surface roughness of <5 nm Sa before the nanoscratching tests.

Nanoscratching tests were conducted using a nanoindentation–scratching system (Nano Indenter G200, KLA Corp., USA) equipped with a Berkovich diamond tip. Fig. 1(a) shows a photograph of the nanoindentation–scratching system. To measure the tip radius, a high-magnification scanning electron microscope (SEM) image of the Berkovich tip was captured from the direction perpendicular to the face (one of the three sides), as shown in Fig. 1(b). The tip radius was estimated to be ~40 nm.

Single and repeated nanoscratching tests were performed with the indenter tip in the face-forward (FF) and edge-forward (EF) directions, respectively, under constant loads. In single scratching, the normal loads were set to 1 and 2 mN, respectively. In the repeated nanoscratching tests, a normal load of 1 mN was used twice to scratch the same path. Furthermore, a single scratching test under an incremental load from 0 to 20 mN was performed in the FF scratching direction. A schematic of the scratching process is shown in Fig. 1(c). For all cases, a pre-scan and a post-scan were performed before and after the designed scratching procedure at a very small load (<8 μN) at a speed of 10 μm/s to detect the initial surface profile and the resulting surface profile. The scratch

Table 1
Experimental parameters for the nanoscratching tests.

Parameter	Constant loading		Incremental loading
Number of scratches	One (single)	Two (repeated)	One (single)
Normal load P (mN)	1, 2	1	0–20
Indenter direction	FF and EF		FF
Length L (μm)	60		200
Speed v (μm/s)	1		
Environment	Dry condition at 23 °C		

speed was 1 μm/s, which was achieved by controlling the positioning table. The experimental parameters of the nanoscratching tests are listed in Table 1.

After the nanoscratching tests, the scratched grooves were characterised using a field-emission SEM (ZEISS MERLIN Compact, Carl Zeiss AG, Germany). A laser micro-Raman spectroscope (inVia Raman, Renishaw Plc., UK) was then used to analyse the possible microstructural changes in the subsurface layer of the workpiece. To further understand the material deformation behaviour related to crystallographic orientation, the subsurface microstructure of the grooves was characterised using a field-emission SEM (ZEISS GeminiSEM 500, Carl Zeiss AG, Germany) equipped with an electron backscatter diffraction (EBSD) detector (EDAX Inc., USA).

3. Results and discussion

3.1. Groove surface morphology of single scratches under constant loads

The SEM images of the grooves scratched in the FF direction under constant loads of 1 and 2 mN are presented in Figure 2(a) and (b), respectively. In both scratched grooves, the surface morphologies varied with grains. In some grains (see location A in Fig. 2(a) and (b)), a lift-up with the width of hundreds of nanometres formed on the polished surface next to the edge of the grooves, which was caused by the lateral crack that generated beneath the material surface and run parallel to the surface. Meanwhile, radial cracks, which are the surface crack traces emanating radially from the scratched groove, were formed on the lift-up. Besides, in the groove, the lateral crack extended upwards to the surface and join the radial crack, resulting in flake-shaped material (indicated as debris in Fig. 2) being peeled off from the bulk and spalling-induced craters being formed in the groove. In some grains (see location B in Fig. 2(a) and (b)), a lift-up formed on the side of the groove, but few cracks were generated in the groove or on the lift-up surface; in some grains (see location C in Fig. 2(a) and (b)), both lift-up formation and crack generation were not significant. In the end region of the groove, slip lines, that is, the intersection lines between the grain's activated slip plane and workpiece surface, which are characterised by a number of fine straight lines parallel to each other [20], were found in front of the indenter, and they were limited to the area within the indenter–workpiece contact width. Consequently, on the polished surface next to the edge of the groove, a few slip lines were observed.

In both scratched grooves it can be observed that periodical fishbone-like patterns were formed along the scratch path. Such fishbone-like patterns have also been reported in nanoscratching experiments using a Berkovich indenter on Lu_2O_3 crystals [21,22] and sapphire [23]. The formation of fishbone-like patterns is considered to be caused by stick–slip motion between the tip of the indenter and the surface of the material, which is the result of the competition between static and kinetic friction coefficients during the nanoscratching process [24,25]. Although the stick–slip motion is not affected by grain orientation, the stick–slip motion will cause the indenter to fluctuate in the loading direction, resulting in the fishbone-like pattern imprinted by the indenter edges in the scratched groove, especially when scratching a soft material under a force-control mode. This is supported by the fact that the angle between the two sides of fishbone-like pattern matches the geometry of the residual indentation imprint (see Fig. 2(a)). Therefore, compared with other materials, the fishbone-like pattern formed on p-ZnSe was more significant. This is because p-ZnSe has a much lower hardness (1.6

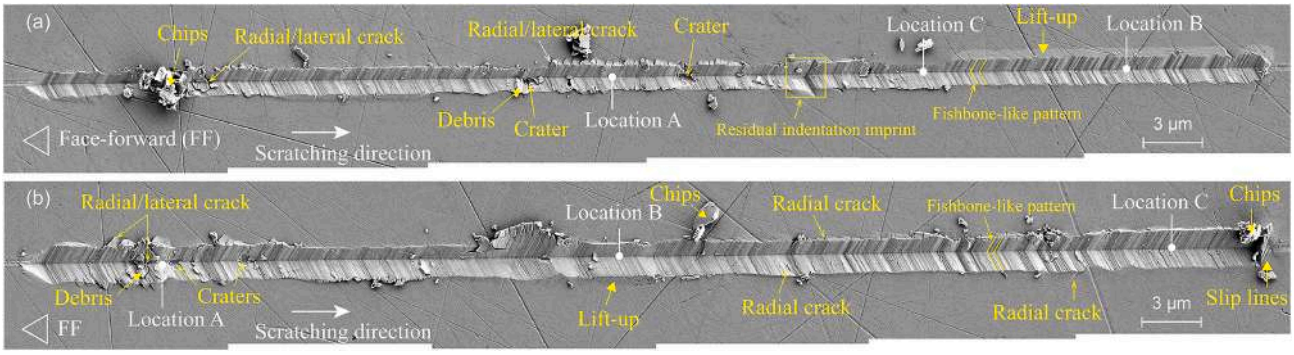

Fig. 2. Stitched SEM images of the groove morphologies resulting from scratching in the FF direction with constant loads of (a) 1 and (b) 2 mN.

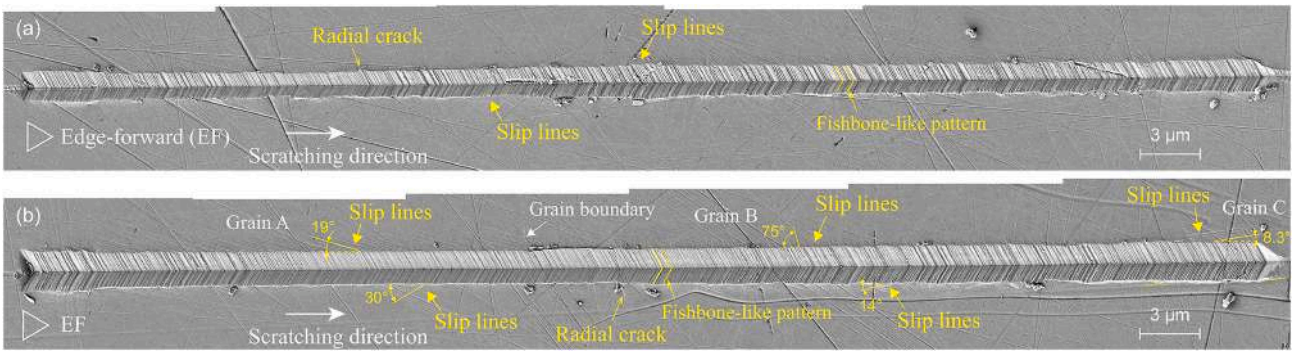

Fig. 3. Stitched SEM images of the groove morphologies resulting from scratching in the EF direction with constant loads of (a) 1 and (b) 2 mN.

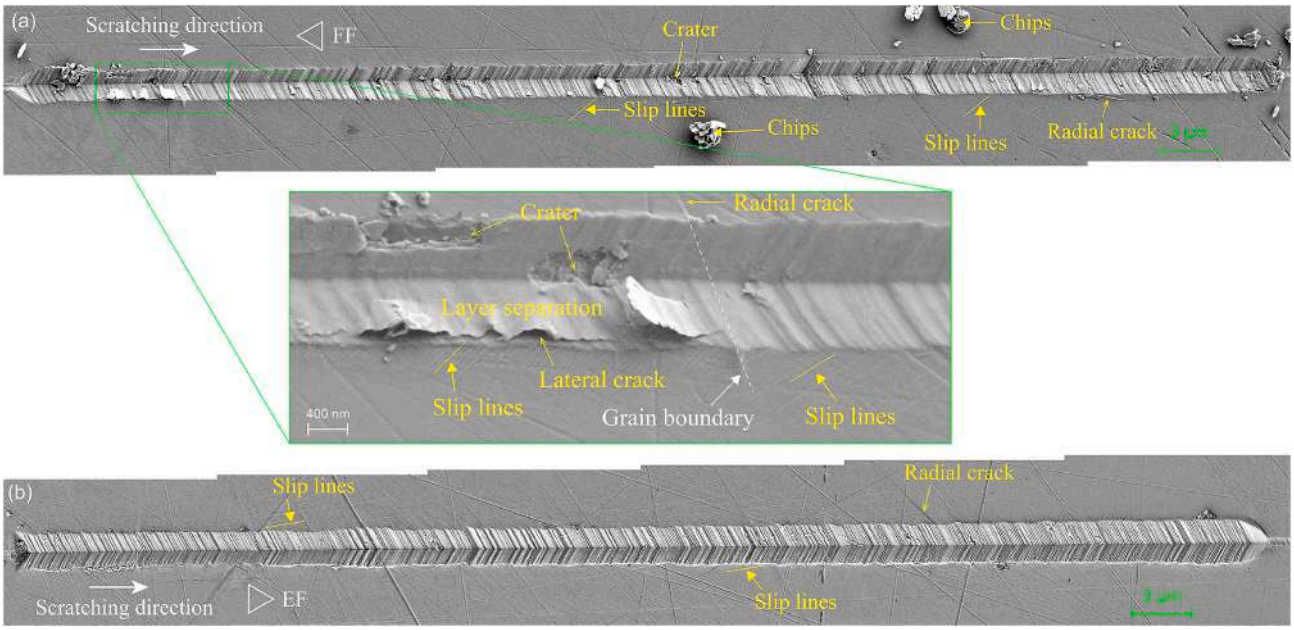

Fig. 4. Stitched SEM images of the groove morphologies resulting from repeated scratching in the (a) FF and (b) EF directions.

± 0.3 GPa) than that of Lu_2O_3 crystal (11.25 GPa) and sapphire (19.4 GPa). It is also worth noting that, by using a spherical indenter tip, a smooth surface free of fishbone-like patterns is created on *p*-ZnSe [20]. This may be attributed to the difference in the indenter tip profile. The radius of the tip profile for a spherical indenter is far greater than that for a Berkovich indenter; therefore, the penetration depth of the spherical

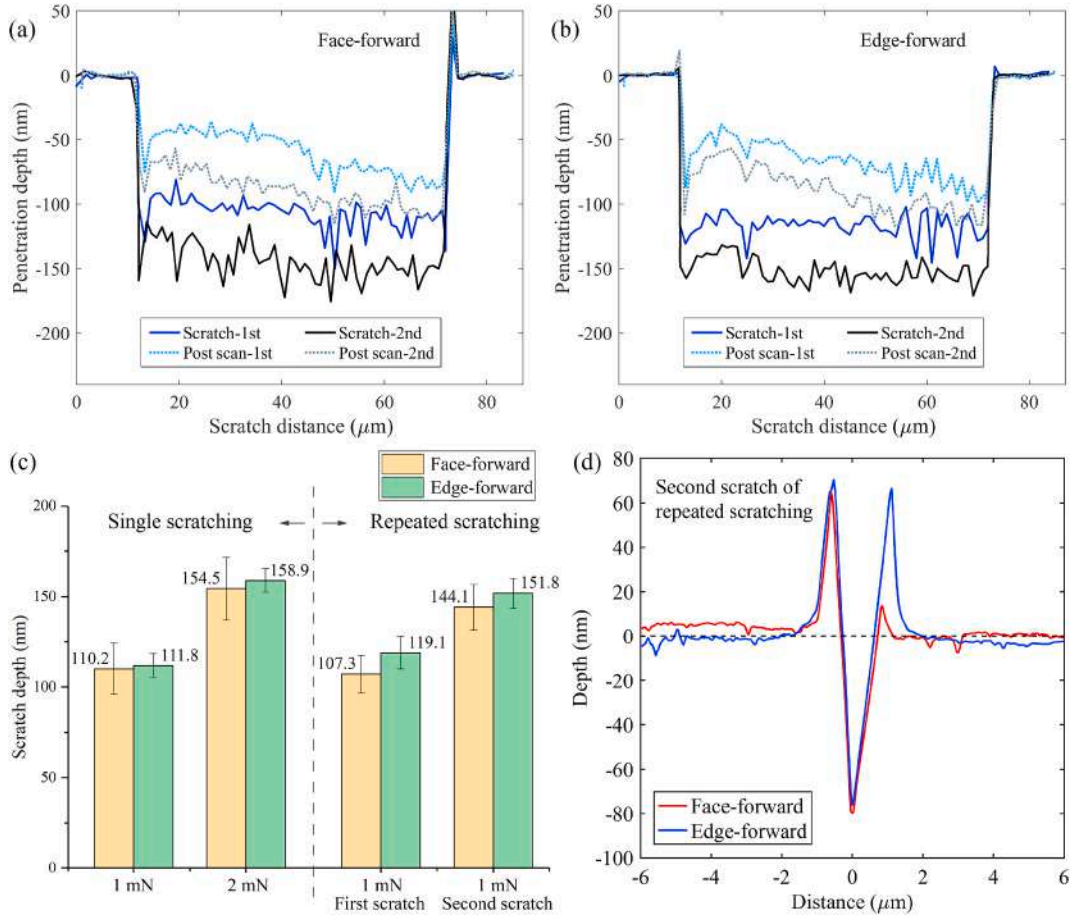

Fig. 5. Scratch depth and residual depth plotted as a function of scratch distance under repeated nanoscratching tests in the (a) FF and (b) EF directions. (c) Comparison of average scratch depth in single and repeated nanoscratching tests. (d) Cross-sectional profiles of the grooves scratched in FF and EF directions in second scratch of repeated nanoscratching.

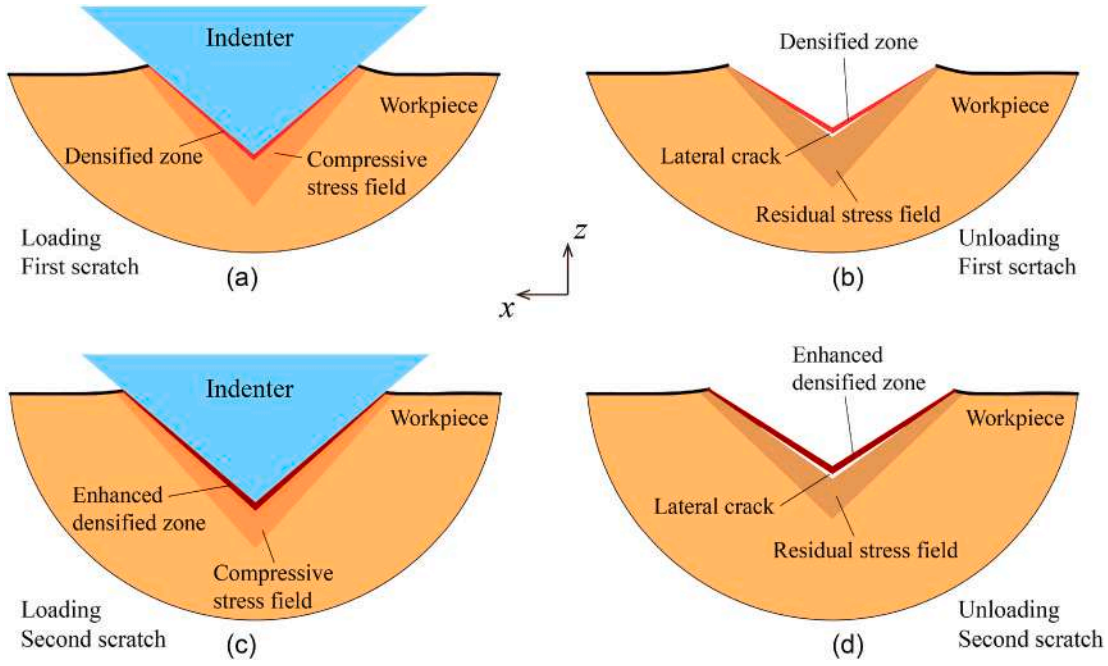

Fig. 6. Schematics illustrating the FF-scratching-induced deformation process at the first (a, b) and the second (c, d) scratch of repeated nanoscratching. (a) and (c) are for loading; (b) and (d) are for unloading.

indenter is much smaller than that of the Berkovich indenter, preventing fishbone-like pattern formation. Similar differences have also been reported in the nanoscratching of Lu_2O_3 crystals [22].

The SEM images of the grooves scratched in the EF direction under constant loads of 1 and 2 mN are presented in Fig. 3(a) and (b), respectively. These surface morphologies were significantly different from those in the FF scratching direction. No craters were found in the entire groove, and only a few radial cracks were observed. However, on the polished surface, it is clearly seen that many slip lines appeared emanating from the edge of the groove. The slip lines abruptly terminate when extending to the grain boundary, as shown in Fig. 3(b), which indicates that the grain boundary stops the slip deformation. Moreover, the slip lines to the left and right edges of the groove were not in the same direction, which indicates that different slip systems were activated to the left and right of the groove. Although the surface morphologies of the grooves in the EF direction are relatively uniform along the scratch path compared with those of the grooves in the FF direction (see Fig. 2), it can still be found that the deformation behaviour of the material is strongly influenced by the crystallographic orientation. This is proven by the fact that the angle of the slip lines to the left or right side of the groove varied with the grains. In addition, it was found that the direction of the fishbone-like pattern in the scratched groove in the EF direction is opposite to that in the FF direction because the indenter was rotated 180° relative to the scratching direction.

3.2. *Effect of repeated scratching*

Fig. 4 shows the SEM images of the grooves created under repeated scratching in the FF and EF directions. For the groove scratched in the FF direction, as shown in Fig. 4(a), craters are observed in the groove that are similar to the craters formed in the single nanoscratching tests (see Fig. 2). The number of cracks propagating on the polished surface was significantly reduced, and the formation of slip lines became obvious. It seems that these few cracks were generated along the boundary, as evidenced by the fact that the directions of the slip lines are different on the two sides of the cracks, as shown in the inset of Fig. 4(a). In addition, it is interesting to note that layer separation occurred in the scratched groove; that is, a large thin layer of material peeled off from the bulk. For the groove scratched in the EF direction, as shown in Fig. 4(b), the surface morphology is very similar to that under single nanoscratching tests (see Fig. 3); in other words, no brittle fracture occurred in the groove, but the slip lines formed on the polished surface varied with the grain orientation, and a few radial cracks were generated along the grain boundaries. This implies that the surface morphology of the groove is barely affected by repeated scratching in the EF direction.

Fig. 5(a) and (b) show the penetration depth curves during repeated constant-load nanoscratching in the FF and EF directions, respectively. The scratch curves and the post-scan curves indicated in the figures correspond to the real-time groove depth during scratching and the residual groove depth after scratching. The curves for the first scratch of the repeated nanoscratching can also be regarded as the curves for the single nanoscratching. It is clearly seen that, whether for single or repeated scratching, there is a significant pile-up formed at the end of the groove in the FF direction, while a relatively small pile-up is found at the end of the groove in the EF direction. This indicates that, in the FF direction, the chips are generated in front of the indenter as a result of the shear deformation of the material; in the EF direction, the ploughing effect, that is, material plastically flowing to the two sides of the indenter, dominates the deformation of the material during the scratching process. Meanwhile, in the EF direction, a small pile-up was formed at the beginning of the groove. This is because, before the indenter starts scratching the workpiece, it gradually presses into the workpiece surface until the load reaches the pre-set value. During this penetration process, the pile-up forms close to the face of the indenter owing to the low-strain-hardening property of the material [26]. Moreover, for all cases, the penetration depths of the post-scan profiles were relatively small at the beginning of the scratch, indicating that the elastic recovery of the material at the beginning of the scratch were larger. This may because the material accumulation in front of the indenter was less significant at the initial stage of the scratching, leading to a relatively slight densification of the subsurface.

Fig. 5(c) compares the average penetration depths of the indenter during single and repeated nanoscratching in both the FF and EF directions. There is a general trend that the average penetration depths of the indenter in the FF direction are less than those in the EF direction under the same load. This might be caused by material in front of the

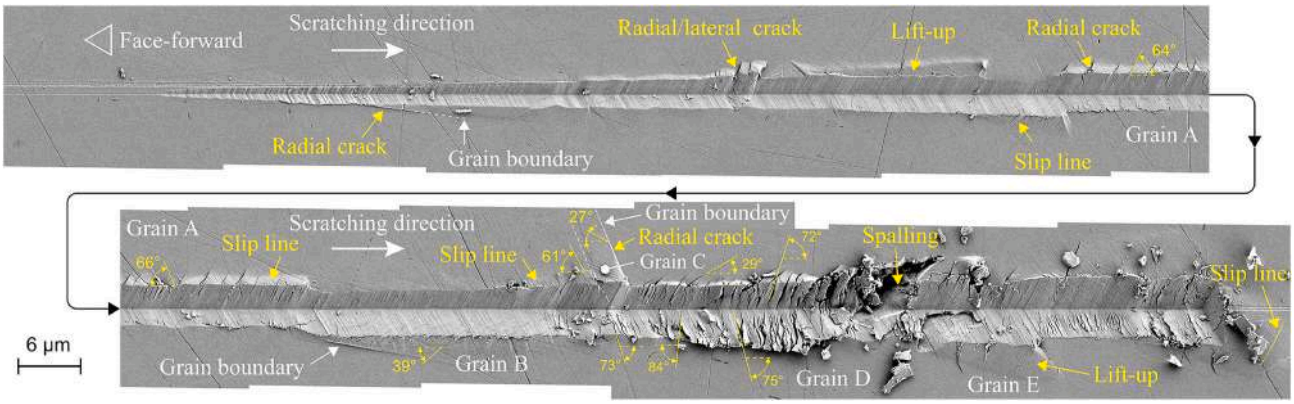

Fig. 7. Stitched SEM image of the groove morphology resulting from incremental load scratching in the FF direction.

indenter face being compacted and accumulated as a result of the sliding of the indenter in the FF direction, consequently leading to an increased resistance force that acts in the opposite direction of both loading and scratching. However, in the EF direction, the indenter tends to push the material to the side, resulting in less resistance force. Meanwhile, the error bars in the FF direction are larger than those in the EF direction, which implies that the fluctuation of the indenter is more severe in the FF direction. However, in the same scratching direction, the penetration depth for the second scratch of repeated nanoscratching was less than that for single scratching with a load of 2 mN. This indicates that the surface hardness of the material after the first scratch of repeated nanoscratching was improved, which might be caused by pressure-induced subsurface densification [27].

Fig. 5(d) presents the cross-sectional profiles of the grooves scratched in FF and EF directions in the second scratch of repeated nanoscratching. For the groove scratched in the FF direction, a significant pile-up was formed on the left side of the groove, which indicates that the material in front of the indenter flowed more easily to the left side during the scratching. This is because the indenter face is vertical to the scratching direction, and the activated slip plane of the grain is asymmetric with respect to the scratching direction. In contrast, for the groove scratched in the EF direction, significant pile-up was formed on both sides with small difference of height, indicating that the left- and right-side faces of the indenter push the material evenly to both sides during the scratching. Moreover, the material removal volume of the scratching in the EF direction is much smaller than that in the FF direction, as evidenced by the fact that the volume of pile-up next to the groove scratched in the EF direction is larger than that in the FF direction, for the same volume of two grooves.

Based on the aforementioned analysis, a schematic model of material deformation during nanoscratching is illustrated in Fig. 6. For the first nanoscratching, during loading, despite the predominant compressive stress below the indenter, part of the material in front of the indenter undergoes elastic and plastic deformation and flows downwards beneath the indenter during the sliding [9]. As a result, subsurface densification occurred in the near-surface layer (see Fig. 6(a)). After the indenter has passed, elastic recovery of the material occurred at the rear of the indenter. This situation is similar to the cutting of brittle materials using a highly negative rake angle tool [28]. Owing to the formation of the densified layer, the tensile stress tends to be enhanced along the boundary between the densified layer and the bulk, generating cracks (see Fig. 6(b)). Therefore, the flake-shaped material was peeled off from the bulk, and spalling-induced craters were formed in the groove, as indicated in Fig. 2.

For the second scratch, during loading, subsurface densification occurs, as in the first scratch of repeated nanoscratching. Moreover, because there is a residual stress zone below the scratch path, which is formed by the first scratch, the densified layer will be enhanced in terms

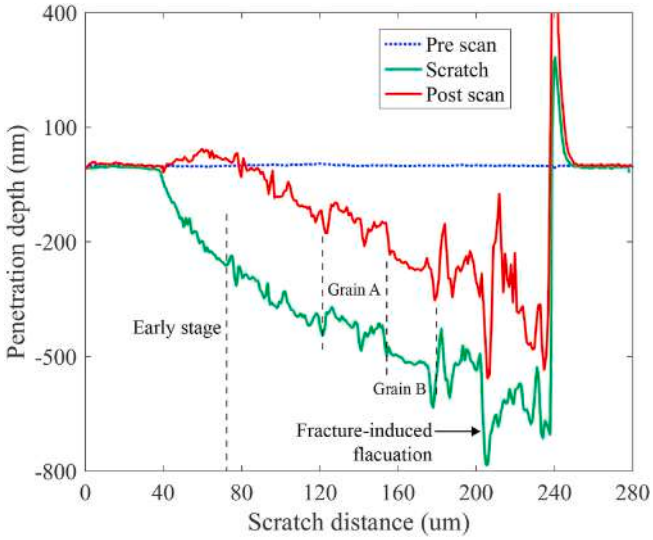

Fig. 8. Penetration depth profiles as a function of the scratch distance under incremental loading.

of thickness and density (see Fig. 6(c)). After the indenter has passed, cracks are generated along the boundary between the enhanced densified layer and the bulk, as a result of the elastic recovery of the bulk (see Fig. 6(d)). Therefore, layer separation characterised by a flake with a larger area was observed in Fig. 4(a). In addition, the separated layer has a wavy shape, indicating that the material of the densified layer was stretched. It can be inferred that sliding friction also applied tensile stress in the scratching direction to the densified layer. However, such a phenomenon was not observed in nanoscratching in the EF direction. This might be because the subsurface densification is less significant as a result of the sideways flow of material, as discussed in Fig. 5(c), and the compressive residual stress is dominant in the subsurface of the scratched groove, which is verified by the Raman spectra presented in Section 3.4.

3.3. *Effect of incremental loading*

Fig. 7 shows the surface morphology of the scratched groove under incremental loading in the FF direction. The corresponding scratch distance versus penetration depth profile is plotted in Fig. 8. As the load gradually increased with the scratch distance, the depth and width of the groove gradually increased. However, because the scratch path of the incremental loading test passes through multiple grains, the critical depth for the ductile-to-brittle transition cannot be precisely quantified. Nonetheless, during the early stage, the material was removed in the

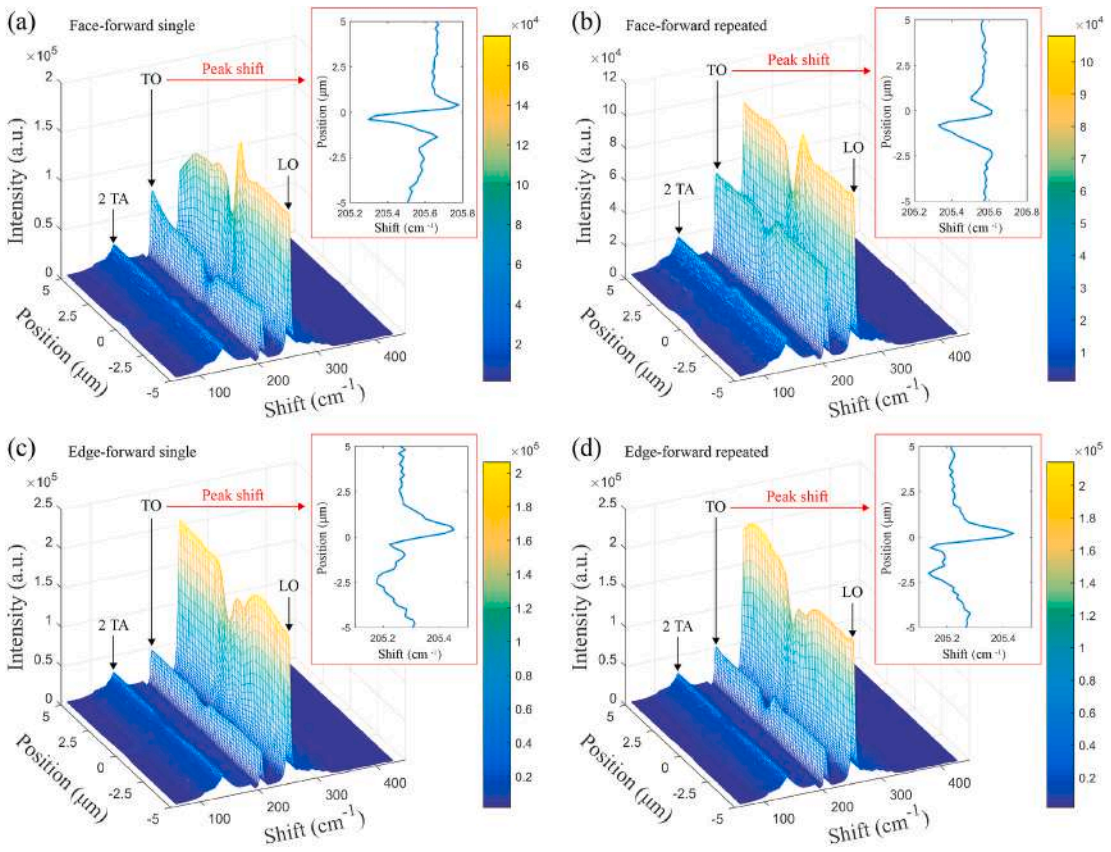

Fig. 9. Raman mapping of scratched grooves under (a) single and (b) repeated nanoscratching in the FF direction and (c) single and (d) repeated nanoscratching in the EF direction. The insets present the Raman peak shift of the TO mode.

ductile mode regardless of the grain orientation. The first observed brittle fracture is a radial crack generated along the grain boundary, which is characterised by a single straight line. This might be caused by the slip systems in two grains being activated along different directions, resulting in intense tensile stresses along the grain boundary [29]. This issue is discussed further in Section 3.5. As the scratch deepens, surface defects, including radial and lateral cracks, lift-ups, and slip lines, are extensively generated; however, the types of surface defects are strongly dependent on the grain orientation. Moreover, the grains with shallower scratch depths (for example, grains A and D) could be damaged more severely than grains with deeper scratch depths (grains B and E). It is noteworthy that significant jumps of penetration depth are observed at the grain boundaries, which indicates that the apparent hardness of the grain varies with its orientation. In the entire scratched groove, the surface morphology with the most serious damage was found in grain D, because many wide radial cracks formed in the groove, and some of them extended to the polished surface. In addition, the intersection of the lateral and radial cracks caused severe spalling, which was also reflected by the violent fluctuation of the penetration depth profile. In grain E, a lift-up with a large area and a large curvature is observed; this appears to be due to surface material being uplifted by the lateral cracks beneath the workpiece surface. At the end of the scratched groove, numerous slip lines were observed in front of the indenter. This supports the viewpoint that, in the FF direction, the material in front of the indenter is mainly subjected to shear stress.

3.4. Subsurface microstructural changes

Raman line mapping was performed to investigate the subsurface microstructural changes in the material caused by nanoscratching. The scanning path for the line mapping was centred on the scratched groove and perpendicular to the scratching direction. The length of the scanning path was 10 μm, with a pitch of 0.2 μm. Fig. 9(a) and (b) show three-dimensional maps of Raman shift versus *X* position versus Raman intensity, which are acquired from the grooves scratched in the FF direction under single and repeated nanoscratching. Fig. 9(c) and (d) show the mapping results acquired from the grooves scratched in the EF direction. For all cases, a transverse acoustic (2 TA) peak at ~140 cm^{-1}, transverse optical (TO) peak at ~206 cm^{-1}, and a longitudinal optical (LO) peak at ~253 cm^{-1} were clearly observed, indicating that there was no phase transformation. This might be because the phase transformation of ZnSe is reversible under hydrostatic or quasi-hydrostatic conditions with pressures of <36 GPa [30]. In this study, the maximum average contact pressure of the scratched grooves in FF and EF directions were ~5.5 and ~3.4 GPa, respectively, under a load of 1 mN. The calculation formulas are described in Appendix A. Therefore, it can be inferred that, during the scratch process, an average contact pressure less than the critical value cannot produce permanent phase transformation, or the pressure-induced phase transformation layer is too thin to be detected by Raman scattering [31]. However, the Raman intensities of the 2 TA, TO, and LO peaks become weak at the centre of the scratched groove, which is attributed to the pressure-induced local lattice distortion in the subsurface of the scratched groove [32].

Moreover, it is worth noting that the shifts of the TO peak at the centre of the grooves move in different directions depending on the scratching direction. In the groove scratched in the FF direction (see Fig. 9(a) and (b)), the TO peaks at the centre of the grooves moved to a lower Raman shift, indicating tensile residual stress in the subsurface of the scratched groove, whereas, in the groove scratched in the EF direction (see Fig. 9(c) and (d)), the TO peaks at the centre of the grooves moved to a higher Raman shift, indicating compressive residual stress in the subsurface of the scratched groove [33]. The former might be

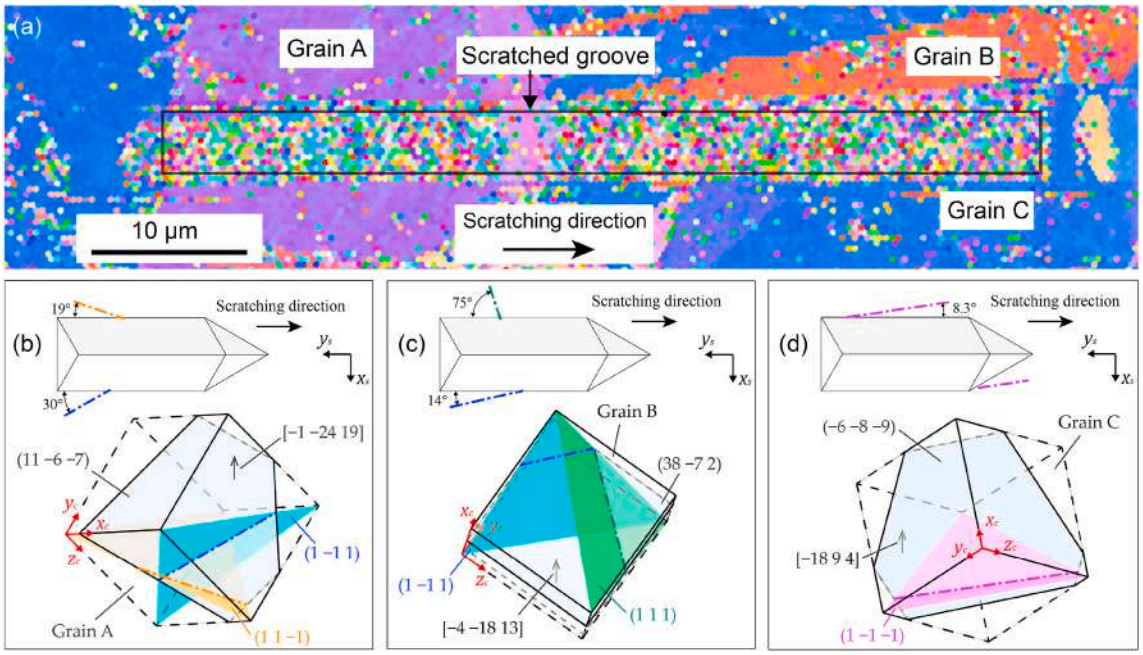

Fig. 10. (a) IPF map of the material around the scratched groove shown in Fig. 3(b). Schematic drawings of the top view of the crystallographic orientation of (b) grain A, (c) grain B, and (d) grain C indicated in (a).

because the shear deformation in front of the indenter face dominates the general mechanism of material removal during the scratching process in the FF direction, as discussed in Fig. 5(a); consequently, sliding friction applies strong tensile stress in the scratching direction, as evidenced by the radial cracks generated in the groove and the wavy, stretched separated layer. The latter might be result from the ploughing effect (in which material plastically flows sideways to the indenter) dominating the deformation of the material during the scratching process in the EF direction, as discussed in Fig. 5(b).

3.5. Effect of grain crystal orientation

To clarify the effect of grain orientation on material deformation, EBSD analysis was conducted to characterise the orientation of the grains around the scratched groove. Fig. 10(a) shows the inverse pole figure (IPF) map of the groove scratched in the EF direction under a load of 2 mN (see Fig. 3(b)). The scratched groove is marked by a square. The scratched area is full of noise points owing to the rough surface of the scratched groove. In addition, the noise points on the polished surface were caused by the poor electrical conductivity of the material. Although there are noise points on the IPF map, the orientation of the grains around the scratched groove could still be extracted and analysed. The crystallographic orientations of three typical grains (grains A, B, and C indicated in Figs. 3(b) and 10(a)) are shown in Fig. 10(b)–(d). Their orientations represented by Miller indices are (11 −6 −7) [−1 −24 19], (38 −7 2) [−4 −18 13], and (−6 −8 −9) [−18 9 4], respectively. It can be clearly seen from Fig. 10(b)–10(d) that the intersection lines of the grain's {111} planes and the workpiece surface have the same slope as the slip lines observed in the SEM image (see Fig. 3(b)). This indicates that slip deformation occurs along the {111} planes, which are well known as the primary slip planes of ZnSe [34].

To rationalise the specific activated slip planes to the left and right sides of the groove detected by SEM and EBSD, the Schmid factor (SF) for each slip system was calculated. It is widely recognised that the SF can reflect the magnitude of the resolved shear stress on slip systems, and the primary slip system will be the system with the greatest SF according to Schmid's law [35,36]. During the scratching process, the material is subjected to a multiaxial stress state, which can be simplified to direct stresses in two directions: (i) load-induced stress, which is normal to the contact planes of the indenter tip, and (ii) sliding friction-induced stress, which is parallel to both the contact planes and workpiece surface [37,38]. The effective SF is the superimposition of the SF determined by the load-induced stress and the SF determined by the sliding friction-induced stress [39]. The formulas for calculating SFs based on the Miller index are presented in Appendix B. Table 2 lists the effective SFs of 12 possible slip systems in grains A, B, and C indicated in both Figs. 3(b) and 10(a). However, it was found that the effective SFs of the observed activated slip systems do not always correspond to the maximum SFs calculated based on the simplified model. There are several possible reasons why slip line formation does not strictly obey Schmid's law: (1) Inherent defects in grains interfered with the activation of slip planes [40,41]; (2) the non-Schmid effect occurred; that is, compressive stresses acting normal to the slip plane affected the shear stress required for dislocation emission [42,43]; and (3) the actual stress distribution during nanoscratching is more complicated than the model considered above.

Fig. 11(a) shows the IPF map of the groove scratched in the FF

Table 2
Effective SFs of the 12 slip systems in grains A, B and C. SFs of the activated slip system are in bold for each grain.

Slip system		SF (grain A)		SF (grain B)		SF (grain C)	
Plane	Direction	Left	Right	Left	Right	Left	Right
(1 1 1)	[1 $\bar{1}$ 0]	0.92	0.54	**0.98**	0.68	0.15	0.35
	[1 0 $\bar{1}$]	0.63	0.96	0.62	0.86	0.18	0.34
	[0 1 $\bar{1}$]	0.35	0.45	0.56	0.26	0.27	0.29
(1 1 $\bar{1}$)	[1 $\bar{1}$ 0]	**1.00**[a]	0.42	0.99[a]	0.55	0.32	0.48
	[1 0 1]	0.34	0.20	0.75	0.37	0.97	0.71
	[0 1 1]	0.90	0.62	0.47	0.33	0.66	1.00[a]
(1 $\bar{1}$ 1)	[1 1 0]	0.17	0.46	0.10	0.77	0.63	0.45
	[1 0 $\bar{1}$]	0.55	**1.02**[a]	0.40	**0.88**[a]	0.18	0.55
	[0 1 1]	0.72	0.84	0.32	0.40	0.54	0.98
($\bar{1}$ 1 1)	[1 1 0]	0.12	0.30	0.12	0.56	0.76	0.34
	[1 0 1]	0.23	0.18	0.52	0.35	**0.98**[a]	**0.50**
	[0 1 $\bar{1}$]	0.20	0.26	0.40	0.21	0.44	0.30

[a] Maximum SF in the 12 slip systems calculated based on the simplified model.

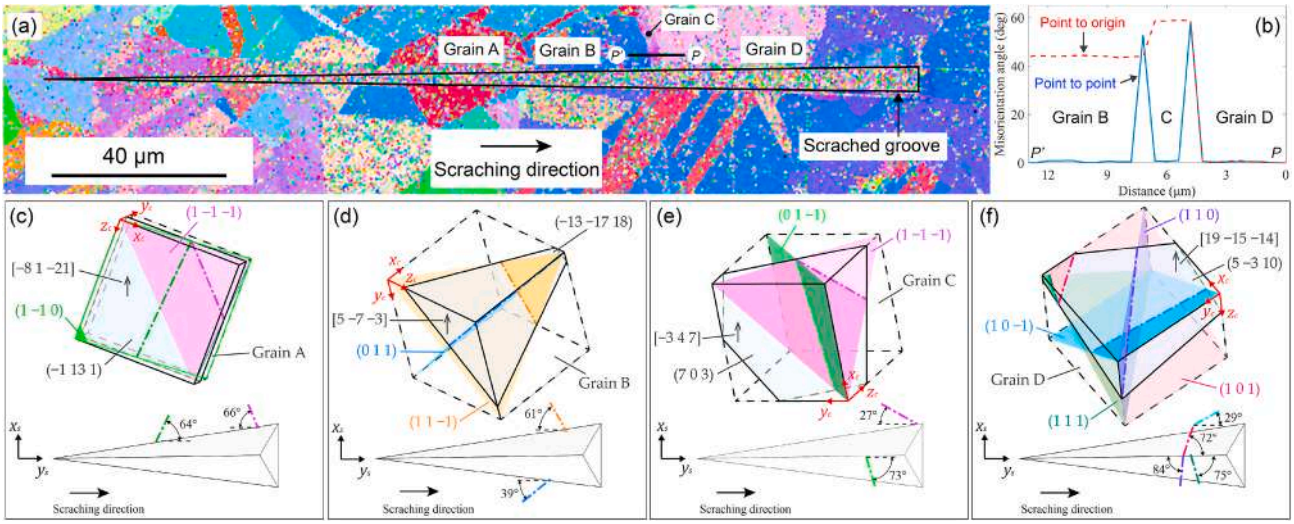

Fig. 11. (a) IPF map of the material around the scratched groove shown in Fig. 7. (b) Misorientation angle profile along line PP' marked in (a). Schematic drawings of the top view of the crystallographic orientation of grains (c) A, (d) B, (e) C, and (f) D indicated in (a).

direction under incremental loading (see Fig. 7). The scratched groove is marked by a triangle. As shown in Fig. 7, a notable radial crack was generated along the grain boundary of grains C and D instead of the grain boundary of grains B and C. To explain this phenomenon, a misorientation angle profile among grains B, C, and D was extracted from the IPF map, as plotted in Fig. 11(b). It was found that grains C and D are twin pairs having a coherent twin boundary around ⟨111⟩, because the misorientation angle between them is 60° [44]. This supports the view that the slip systems in twin grains are activated along different directions and consequently intense tensile stresses are generated along their boundary, causing the radial crack.

The crystallographic orientations of four typical grains (grains A, B, C, and D indicated in both Figs. 7 and 11(a)) are shown in Fig. 11(c)–(f). The intersecting lines between the crystal planes and the workpiece surface are plotted in the same way as in Fig. 10. The orientations of the four grains represented by Miller indices are (−1 13 1) [−8 1 −21], (−13 −17 18) [5 −7 −3], (7 0 3) [−3 4 7], and (5 −3 10) [19 −15 −14], respectively. In most cases, slips occur along the {111} planes, and cracks are generated along the {110} planes. However, slips forming along the [0 1 1] plane (in grain B) and cracks forming along the (1 1 1) plane (in grain D) were also observed. This implies that the {111} planes can be the primary slip plane and secondary cleavage plane of the ZnSe crystal and that the {110} planes can be the primary cleavage plane and secondary slip plane of the ZnSe crystal.

4. Conclusions

Nanoscratching tests were conducted on *p*-ZnSe using a sharp Berkovich indenter in both the FF and EF scratching directions. The material deformation behaviour, including surface defects and subsurface microstructural changes caused by nanoscratching, was investigated. The main conclusions are summarised as follows:

(1) Shear deformation in front of the indenter is the predominant deformation behaviour in the scratch in the FF direction, whereas side flow of the material dominates the deformation behaviour during scratching in the EF direction.
(2) A fishbone-like pattern was observed in the scratched grooves under all loads. The main reason for this is the stick–slip motion enhanced by the sharp geometry of the indenter and the low hardness of the material.
(3) Layer separation was observed in the scratched groove after repeated nanoscratching in the FF direction. A subsurface densification layer was generated by the negative rake angle of the indenter, and lateral cracks were generated between this layer and the bulk.
(4) No phase transformation was detected in the scratched grooves; rather, local lattice distortion occurred in the subsurface layer. Tensile residual stress was dominant in the subsurface of the scratched groove in the FF direction, whereas compressive residual stress was dominant in the subsurface of the scratched groove in the EF direction.
(5) The surface morphologies of the scratched grooves were strongly dependent on the grain orientation. Notable radial cracks were likely to be generated along the twin boundaries. The {111} planes can act as the primary slip plane and secondary cleavage plane of the ZnSe crystal, and the {110} planes can act the primary cleavage plane and secondary slip planes of the ZnSe crystal.

The results of this study provide a reference for understanding the fundamental material removal mechanisms of soft brittle polycrystals in various abrasive machining processes, such as grinding, lapping, and polishing. As the observed slip lines cannot be explained by the simplified Schmid's law, further verification of the model is required in the future to accurately predict the activation of slip systems.

Declaration of competing interest

The authors declare that they have no known competing financial interests or personal relationships that could have appeared to influence the work reported in this paper.

Acknowledgements

This work has been partially supported by KLL Ph.D. Program Research Grant of Keio University. Thanks are extended to Mr. Tomoyuki Takano and Mrs. Kawori Tanaka of Central Testing Center of Keio University for their technical assistance in SEM and EBSD observations as well as sample preparation.

Appendix A. Calculation of average contact pressure

The average contact pressure p_{avg} during scratching is calculated as the normal load P divided by the projected area of the indenter in contact with the workpiece, S:

$$p_{avg} = P/S. \tag{A.1}$$

The projected area of the indenter in contact with the workpiece in the FF and EF directions is shown in Figs. A1 and A2, respectively.

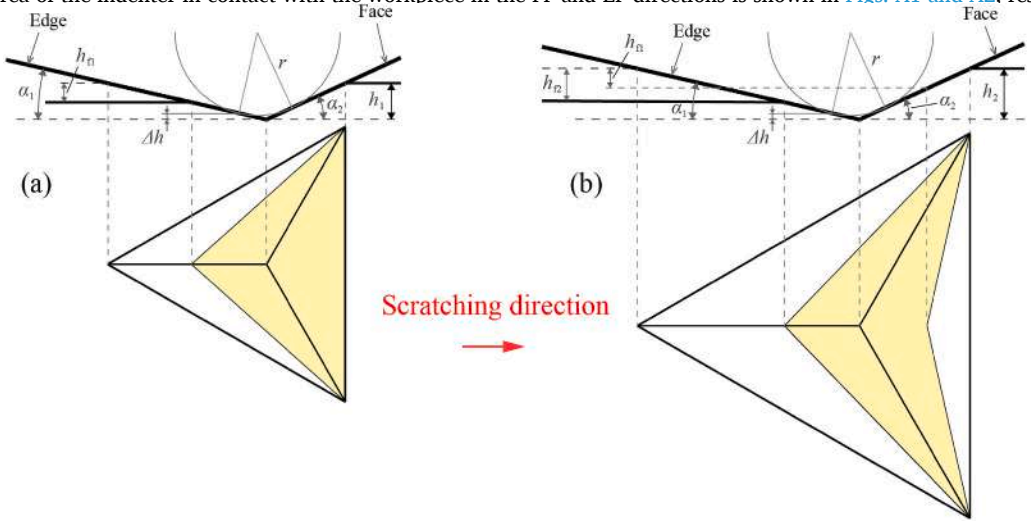

Fig. A1. Projected area of the indenter in contact with the workpiece in the FF direction under (a) single and (b) repeated nanoscratching.

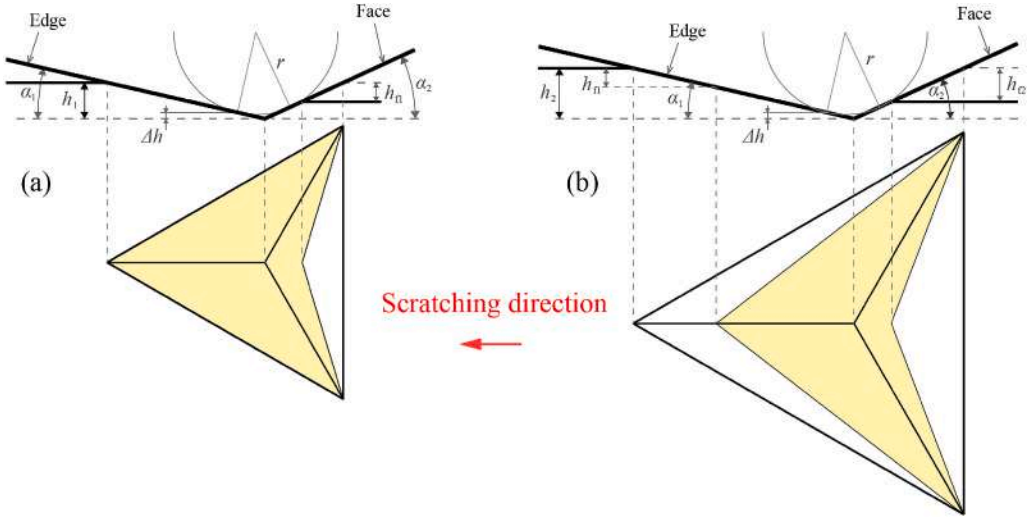

Fig. A2. Projected area of the indenter in contact with the workpiece in the EF direction under (a) single and (b) repeated nanoscratching.

For the case of scratching in the FF direction, the projected area of the first scratch of repeated nanoscratching (also the projected area of the single nanoscratching), $S_{FF\text{-}1}$, can be calculated from [45].

$$S_{FF-1} = \frac{\sqrt{3}}{4}\tan^2\left(\frac{\pi}{2} - \alpha_1\right)(h_1 + \Delta h)\left(3h_1 + 3\Delta h - 2h_{f1}\right), \tag{A.2}$$

where α_1 is 12.95° for the Berkovich indenter; h_1 and h_{f1} are the penetration depth and residual depth for the first scratch of repeated nanoscratching, respectively; and Δh is the difference between the actual and ideal depths, which can be calculated as follows:

$$\Delta h = r\cos^{-1}\left(\frac{\alpha_1 + \alpha_2}{2}\right)\cos\left(\frac{\alpha_2 - \alpha_1}{2}\right) - r, \tag{A.3}$$

where α_2 is 24.75° for the Berkovich indenter and r is the tip radius of the Berkovich indenter.

The projected area of the second scratch of the repeated nanoscratching, $S_{FF\text{-}2}$, can be calculated [45].

$$S_{FF-2} = \frac{\sqrt{3}}{2}\tan\left(\frac{\pi}{2}-\alpha_1\right)(h_2+\Delta h)\left((h_2+\Delta h-h_{f1})\tan\left(\frac{\pi}{2}-\alpha_2\right)\right. \\ \left.+(h_2+\Delta h-h_{f2})\tan\left(\frac{\pi}{2}-\alpha_1\right)\right), \tag{A.4}$$

where h_2 and h_{f2} are the penetration depth and residual depth for the second scratch of repeated nanoscratching, respectively.

For the scratch in the EF direction, the projected area of the first scratch of repeated nanoscratching (as well as the projected area of the single nanoscratching), $S_{EF\text{-}1}$, can be expressed as follows:

$$S_{EF-1} = \frac{\sqrt{3}}{3}\left(\frac{h_1+\Delta h}{\tan\alpha_1}+\frac{h_1+\Delta h-h_{f1}}{\tan\alpha_2}\right)\left(\frac{h_1+\Delta h}{\tan\alpha_1}+\frac{h_1+\Delta h}{\tan\alpha_2}\right). \tag{A.5}$$

The projected area for the second scratch of the repeated nanoscratching, $S_{EF\text{-}2}$, can be expressed as follows:

$$S_{EF-2} = \frac{\sqrt{3}}{3}\left(\frac{h_2+\Delta h}{\tan\alpha_1}+\frac{h_2+\Delta h}{\tan\alpha_2}\right)\left(\frac{h_2+\Delta h-h_{f1}}{\tan\alpha_1}+\frac{h_2+\Delta h-h_{f2}}{\tan\alpha_2}\right). \tag{A.6}$$

Appendix B. Calculation of SFs

Fig. B1 shows a schematic of the simplified multiaxial stress state of the material induced by the Berkovich indenter during EF scratching [37,38].

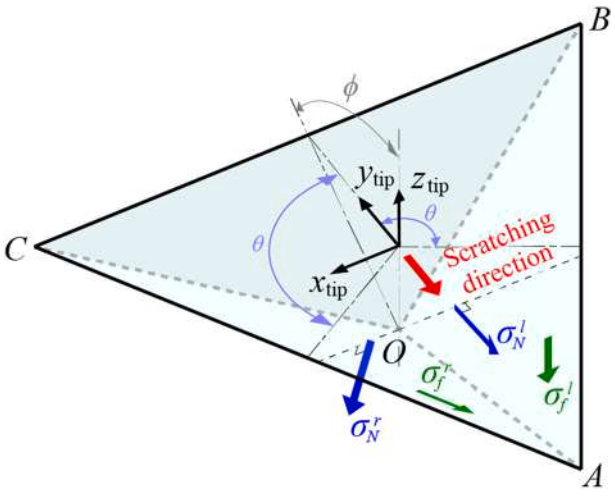

Fig. B1. Schematic of the simplified multiaxial stress state of material induced by a Berkovich indenter during EF scratching.

The normal vectors of the *AOB* and *AOC* planes, which are the directions of the load-induced stresses that act from the left- and right-side faces of the Berkovich indenter, can be expressed as

$$\sigma_{N-Tip}^{l} = [0 \quad 1 \quad 0] \times R_x \times R_z^l, \tag{B.1}$$

$$\sigma_{N-Tip}^{r} = [0 \quad 1 \quad 0] \times R_x \times R_z^r, \tag{B.2}$$

where R_x is the rotation matrix that rotates the unit vector in the direction of the y axis around the x axis by ϕ, which will make the rotated vector perpendicular to the *BOC* plane, and R_z^l and R_z^r are the rotation matrices that rotate the *BOC* plane around the z axis by θ, which will make the *BOC* plane coincide with the *AOB* and *AOC* planes, respectively.

The rotation matrixes R_x, R_z^l, and R_z^r are expressed as follows:

$$R_x = \begin{bmatrix} 1 & 0 & 0 \\ 0 & \cos\phi & \sin\phi \\ 0 & -\sin\phi & \cos\phi \end{bmatrix}, \tag{B.3}$$

$$R_z^l = \begin{bmatrix} \cos\theta & \sin\theta & 0 \\ -\sin\theta & \cos\theta & 0 \\ 0 & 0 & 1 \end{bmatrix}, \tag{B.4}$$

$$R_z^r = \begin{bmatrix} \cos\theta & -\sin\theta & 0 \\ \sin\theta & \cos\theta & 0 \\ 0 & 0 & 1 \end{bmatrix}, \tag{B.5}$$

where ϕ is 65.25° and θ is 120° for the Berkovich indenter.

The vectors of lines *BA* and *CA*, which are the directions of the sliding-friction-induced stresses that act from the left- and right-side faces of the Berkovich indenter, can be expressed as

$$\sigma_{f-Tip}^{l} = \begin{bmatrix} 1 & -\sqrt{3} & 0 \end{bmatrix}, \tag{B.6}$$

$$\sigma_{f-Tip}^{r} = \begin{bmatrix} -1 & -\sqrt{3} & 0 \end{bmatrix}. \tag{B.7}$$

Fig. B2 shows a schematic of the relationship between the sample coordinate system (SCS) and the crystal coordinate system (CCS). The (*h k l*) plane in the CCS is parallel to the (0 0 1) plane in the SCS, and the [*u v w*] vector in the CCS is parallel to the [1 0 0] vector in the SCS. The coordinate system of the indenter coincides with the SCS. Therefore, σ_{N-Tip} and σ_{f-Tip} in the CCS can be expressed as

$$\sigma_{N-Cry} = \sigma_{N-Tip} \times \mathbf{g}^{-1}, \tag{B.8}$$

$$\sigma_{f-Cry} = \sigma_{f-Tip} \times \mathbf{g}^{-1}, \tag{B.9}$$

where **g** is the rotation matrix, which can be expressed as

$$\mathbf{g} = \begin{bmatrix} u & r & h \\ v & s & k \\ w & t & l \end{bmatrix}, \tag{B.10}$$

$$[r \quad s \quad t] = [h \quad k \quad l] \times [u \quad v \quad w]. \tag{B.11}$$

Therefore, the angle between the stress vector and the slip plane normal, φ, and the angle between the stress vector and the slip direction, λ, can be expressed as

$$\varphi_i = \arcsin\left(\frac{|\sigma_{i-Cry} \cdot \mathbf{SP}|}{|\sigma_{i-Cry}| \ |\mathbf{SP}|}\right) \quad (i = N, \ f), \tag{B.12}$$

$$\lambda_i = \arccos\left(\frac{|\sigma_{i-Cry} \cdot \mathbf{SD}|}{|\sigma_{i-Cry}| \ |\mathbf{SD}|}\right) \quad (i = N, \ f), \tag{B.13}$$

where **SP** is the slip plane normal and **SD** is the slip direction.

Because the effective SF is the superimposition of the SF determined by the load-induced stress and the SF determined by the sliding-friction-induced stress, the effective SF can be expressed as

$$\mathrm{SF}_{\mathrm{eff}} = \cos\varphi_N^j \cos\lambda_N^j + \mu \cos\varphi_f^j \cos\lambda_f^j \quad (j = l, \ r), \tag{B.14}$$

where μ is the friction coefficient. The effective SFs listed in Table 2 were calculated using $\mu = 0.2$, which makes the results of the simplified model closest to the observed results.

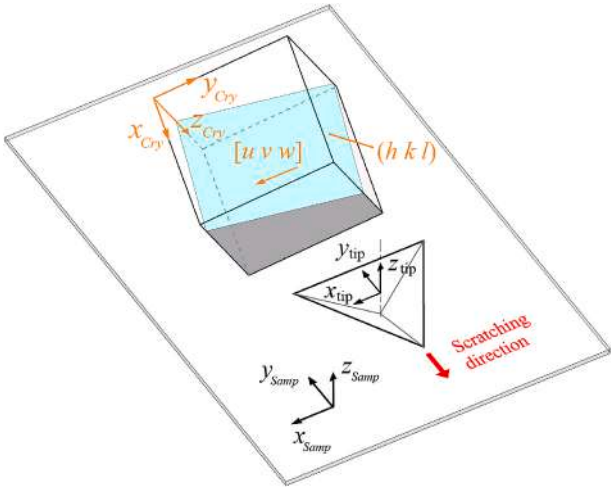

Fig. B2. Schematic of the relationship between the sample coordinate system and the crystal coordinate system.

References

[1] Yan J, Tamaki JI, Syoji K, Kuriyagawa T. Single-point diamond turning of CaF2 for nanometric surface. Int J Adv Manuf Technol 2004;24:640–6.
[2] Qu M, Xie G, Jin T, Cai R, Lu A. Realization of high efficiency and low damage machining of anisotropic KDP crystal by grinding. Precis Eng 2019;55:464–73.
[3] Fang FZ, Venkatesh VC, Zhang GX. Diamond turning of soft semiconductors to obtain nanometric mirror surfaces. Int J Adv Manuf Technol 2002;19:637–41.
[4] Irwan R, Huang H, Zheng HY, Wu H. Mechanical properties and material removal characteristics of soft-brittle HgCdTe single crystals. Mater Sci Eng, A 2013;559:480–5.
[5] Zhang Z, Meng Y, Guo D, Wu L, Tian Y, Liu R. Material removal mechanism of precision grinding of soft-brittle CdZnTe wafers. Int J Adv Manuf Technol 2010;46:563–9.
[6] Zhang Z, Yan J, Kuriyagawa T. Manufacturing technologies toward extreme precision. Int J Extreme Manuf 2019;1:022001.
[7] Huang W, Yan J. Fundamental investigation of diamond cutting of micro V-shaped grooves on a polycrystalline soft-brittle material. J Manuf Mater Process 2021;5:17.
[8] Zong WJ, Cao ZM, He CL, Xue CX. Theoretical modelling and FE simulation on the oblique diamond turning of ZnS crystal. Int J Mach Tool Manufact 2016;100:55–71.
[9] Huang W, Yan J. Surface formation mechanism in ultraprecision diamond turning of coarse-grained polycrystalline ZnSe. Int J Mach Tool Manufact 2020;153:103554.
[10] Yan J, Takahashi Y, Tamaki J, Kubo A, Kuriyagawa T, Sato Y. Ultraprecision machining characteristics of poly-crystalline germanium. JSME 2006;49:63–9. International Journal Series C Mechanical Systems, Machine Elements and Manufacturing.
[11] Li C, Zhang F, Piao Y. Strain-rate dependence of surface/subsurface deformation mechanisms during nanoscratching tests of GGG single crystal. Ceram Int 2019;45:15015–24.
[12] Huang H, Li X, Mu D, Lawn BR. Science and art of ductile grinding of brittle solids. Int J Mach Tool Manufact 2021;161:103675.
[13] Li W, Li Z, Yang J, Ren Y, Jiao Y, Hegab H, Mahmoud Ibrahim AM. Modeling of the removal mechanism of monocrystalline silicon-based on phase change-dislocation theory and its edge chipping damage during micro-grinding. Precis Eng 2021;71:103–18.
[14] Zhu Y, Ding W, Rao Z, Yang C. Micro-fracture mechanism of polycrystalline CBN grain during single grain scratching tests based on fractal dimension analysis. Precis Eng 2019;59:26–36.
[15] Xu N, Han W, Wang Y, Li J, Shan Z. Nanoscratching of copper surface by CeO2. Acta Mater 2017;124:343–50.
[16] Axinte D, Butler-Smith P, Akgun C, Kolluru K. On the influence of single grit micro-geometry on grinding behavior of ductile and brittle materials. Int J Mach Tool Manufact 2013;74:12–8.
[17] Borrero-López O, Vodenitcharova T, Quadir MZ, Hoffman M. Scratch fracture of polycrystalline silicon wafers. J Am Ceram Soc 2015;98:2587–94.
[18] Ghosh D, Subhash G, Radhakrishnan R, Sudarshan TS. Scratch-induced microplasticity and microcracking in zirconium diboride–silicon carbide composite. Acta Mater 2008;56:3011–22.
[19] Csanádi T, Kovalčíková A, Dusza J. Orientation-dependent nanoscratch resistance of zirconium diboride ceramic grains. Int J Refract Metals Hard Mater 2017;65:45–51.
[20] Huang W, Yan J. Chip-free surface patterning of toxic brittle polycrystalline materials through micro/nanoscale burnishing. Int J Mach Tool Manufact 2021:103688.
[21] Zhang S, Guo X, Jin Z, Kang R, Guo D. Material removal characteristics of precorroded Lu2O3 laser crystals and elastic deformation model during nanoscratch process. Tribol Int 2020;143:106027.
[22] Li C, Zhang F, Wu Y, Zhang X. Influence of strain rate effect on material removal and deformation mechanism based on ductile nanoscratch tests of Lu2O3 single crystal. Ceram Int 2018;44:21486–98.
[23] Huang L, Bonifacio C, Song D, Benthem KV, Mukherjee AK, Schoenung JM. Investigation into the microstructure evolution caused by nanoscratch-induced room temperature deformation in M-plane sapphire. Acta Mater 2011;59:5181–93.
[24] Huang L, Zhang Z, Zhao Y, Yao W, Mukherjee AK, Schoenung JM. Scratch-induced deformation in fine- and ultrafine-grained bulk alumina. Scripta Mater 2010;63:528–31.
[25] Carreon AH, Funkenbusch PD. Nanoscale properties and deformation of human enamel and dentin. J Mech Behav Biomed Mater 2019;97:74–84.
[26] Wang Y, Raabe D, Klüber C, Roters F. Orientation dependence of nanoindentation pile-up patterns and of nanoindentation microtextures in copper single crystals. Acta Mater 2004;52:2229–38.
[27] Lawn B, Wilshaw R. Indentation fracture: principles and applications. J Mater Sci 1975;10:1049–81.
[28] Yan J, Syoji K, Kuriyagawa T. Ductile-brittle transition at large negative tool rake angles. J Jpn Soc Precis Eng 2000;66:1130–4.
[29] Tang F, Zhang L. Subsurface nanocracking in monocrystalline Si (001) induced by nanoscratching. Eng Fract Mech 2014;124–125:262–71.
[30] Pu C, Dai L, Li H, Hu H, Liu K, Yang L, Hong M. Pressure-induced phase transitions of ZnSe under different pressure environments. AIP Adv 2019;9:025004.
[31] Yan J, Asami T, Kuriyagawa T. Nondestructive measurement of machining-induced amorphous layers in single-crystal silicon by laser micro-Raman spectroscopy. Precis Eng 2008;32:186–95.
[32] Cheng B, Lou H, Sarkar A, Zeng Z, Zhang F, Chen X, Tan L, Prakapenka V, Greenberg E, Wen J, Djenadic R, Hahn H, Zeng Q. Pressure-induced tuning of lattice distortion in a high-entropy oxide. Commun Chem 2019;2:114.
[33] Niitsu K, Yan J. Effects of deep subsurface damages on surface nanostructure formation in laser recovery of grinded single-crystal silicon wafers. Precis Eng 2020;62:213–22.
[34] Yonenaga I, Watanabe K, Itoh S, Fujiwara S. Dynamics and characters of dislocations in ZnSe. J Mater Sci 2006;41:2601–4.
[35] Mizumoto Y, Kakinuma Y. Revisit of the anisotropic deformation behavior of single-crystal CaF2 in orthogonal cutting. Precis Eng 2018;53:9–16.
[36] Wang Z, Zhang J, Xu Z, Zhang J, Li G, Zhang H, Li Z, Hassan HU, Fang F, Hartmaier A, Yan Y, Sun T. Crystal anisotropy-dependent shear angle variation in orthogonal cutting of single crystalline copper. Precis Eng 2020;63:41–8.
[37] Meng B, Yuan D, Zheng J, Qiu P, Xu S. Tip-based nanomanufacturing process of single crystal SiC: ductile deformation mechanism and process optimization. Appl Surf Sci 2020;500:144039.
[38] Geng Y, Zhang J, Yan Y, Yu B, Geng L, Sun T. Experimental and theoretical investigation of crystallographic orientation dependence of nanoscratching of single crystalline copper. PloS One 2015;10:e0131886.
[39] Luo JR, Godfrey A, Liu W, Liu Q. Twinning behavior of a strongly basal textured AZ31 Mg alloy during warm rolling. Acta Mater 2012;60:1986–98.
[40] Hu X, Ni Y, Zhang Z. Atomistic study of interactions between intrinsic kink defects and dislocations in twin boundaries of nanotwinned copper during nanoindentation. Nanomaterials 2020;10.
[41] Zheng B, Fu F, Wang LL, Wang J, Du L, Du H. Effect of defects on the mechanical deformation mechanisms of metal–organic framework-5: a molecular dynamics investigation. J Phys Chem C 2018;122:4300–6.
[42] Spearot DE, Tschopp MA, Jacob KI, McDowell DL. Tensile strength of ⟨100⟩ and ⟨110⟩ tilt bicrystal copper interfaces. Acta Mater 2007;55:705–14.
[43] Cai Y, Wu HA, Luo SN. A loading-dependent model of critical resolved shear stress. Int J Plast 2018;109:1–17.
[44] Jung J, Yoon JI, Kim JG, Latypov MI, Kim JY, Kim HS. Continuum understanding of twin formation near grain boundaries of FCC metals with low stacking fault energy. Npj Comput Mater 2017;3:21.
[45] Li C, Zhang F, Wang X, Rao X. Repeated nanoscratch and double nanoscratch tests of Lu2O3 transparent ceramics: material removal and deformation mechanism, and theoretical model of penetration depth. J Eur Ceram Soc 2018;38:705–18.